Termination-dependent electronic structure and atomic-scale screening behavior of the Cu 2 O(111) surface

Alexander Gloystein, Niklas Nilius, Claudine Noguera, Jacek Goniakowski

▶ **To cite this version:**

Alexander Gloystein, Niklas Nilius, Claudine Noguera, Jacek Goniakowski. Termination-dependent electronic structure and atomic-scale screening behavior of the Cu 2 O(111) surface. Journal of Physics: Condensed Matter, 2021, 33 (48), pp.484001. ⟨10.1088/1361-648X/ac2534⟩. ⟨hal-03364969⟩

HAL Id: hal-03364969

https://hal.science/hal-03364969v1

Submitted on 7 Oct 2021

HAL is a multi-disciplinary open access archive for the deposit and dissemination of scientific research documents, whether they are published or not. The documents may come from teaching and research institutions in France or abroad, or from public or private research centers.

L'archive ouverte pluridisciplinaire **HAL**, est destinée au dépôt et à la diffusion de documents scientifiques de niveau recherche, publiés ou non, émanant des établissements d'enseignement et de recherche français ou étrangers, des laboratoires publics ou privés.

HAL Authorization

TERMINATION-DEPENDENT ELECTRONIC STRUCTURE AND ATOMIC-SCALE SCREENING BEHAVIOR OF THE $Cu_2O(111)$ SURFACE

*Alexander Gloystein, Niklas Nilius**

Carl von Ossietzky Universität, Institut für Physik, D-26111 Oldenburg, Germany

*Claudine Noguera, Jacek Goniakowski**

CNRS-Sorbonne Université, UMR 7588, INSP, F-75005 Paris, France

E-mail : Niklas.Nilius@uni-oldenburg.de, Jacek.Goniakowski@insp.jussieu.fr

ABSTRACT

By combining differential conductance (dI/dV) spectroscopy with a scanning tunneling microscope and hybrid density functional theory simulations we explore the electronic characteristics of the (1×1) and (√3×√3)R30° terminations of the $Cu_2O(111)$ surface close to thermodynamic equilibrium. Although frequently observed experimentally, the composition and atomic structure of these two terminations remain controversial. Our results show that their measured electronic signatures, such as the conduction band onset deduced from dI/dV measurements, the bias-dependent appearance of surface topographic features, as well as the work function retrieved from field emission resonances unambiguously confirm their recent assignment to a (1×1) Cu-deficient and a (√3×√3)R30° nano-pyramidal reconstruction. Moreover, we demonstrate that due to a different localization of the screening charges at these Cu-deficient terminations, their electronic characteristics qualitatively differ from those of the stoichiometric (1×1) and O-deficient (√3×√3) terminations often assumed in the literature. As a consequence, aside from the topographic differences recently pointed out, also their electronic characteristics may contribute to a radical change in the common perception of the $Cu_2O(111)$ surface reactivity.

1. Introduction

Cuprous oxide Cu_2O is a stable compound formed in the first stages of copper oxidation. It is one of the few p-type conductive oxides; it possesses a band gap in the visible range, and an exceptionally large exciton binding energy.[1,2] It finds applications in photovoltaics and photocatalysis and is expected to play a central role in the development of all-oxide electronic devices.[3,4,5] Its surface reactivity has attracted considerable attention as well and various adsorption and reaction processes have been addressed by either theory or experiment, such as de-hydrogenation of methanol,[6] NO oxidation,[7] O_2 dissociation,[8] water binding and CO_2 adsorption.[9,10] The obtained results were typically explained with the impact of dangling bond states due to unsaturated surface Cu ions and O vacancies. However, neither the presence of such surface features nor their role in the surface reactivity could be proven experimentally. Consequently, there is a clear need to re-examine the structural and electronic properties of the $Cu_2O(111)$ surface.

Electron diffraction (LEED) measurements on $Cu_2O(111)$ systematically revealed both, a (1×1) and a (√3×√3) pattern,[11,12,13,14] and numerous density functional theory (DFT) studies have been initiated to rationalize these findings. The proposed $Cu_2O(111)$ surface models hereby ranged from a stoichiometric[15] and Cu-depleted (1×1) termination,[16] to configurations with 1/3rd of the surface oxygen ions removed to realize the observed (√3×√3)R30° reconstruction.[10]

We have recently developed an experimental route to grow Cu_2O films via high-pressure Cu oxidation in 50 mbar O_2.[17] The high quality of these samples combined with state-of-the-art DFT calculations allowed us to build a new atomistic model for the (√3×√3)R30° reconstruction.[18] It is based on Cu_4O nano-pyramids bound to every third surface Cu-O six ring, which show up with a distinct shamrock shape in the respective STM images. This surface configuration is found to be by far more stable than any other model existing in the literature. Moreover, it is the only one to correctly account for the observed location of the shamrock maxima in the center of the Cu-O rings, for the orientation of their lobes and the mainly topographic nature of the STM contrast.

In the present experimental and computational study, we provide insight into the electronic structure of the (√3×√3)R30° reconstruction of $Cu_2O(111)$. The excellent agreement between hybrid DFT simulations and measured electronic signatures, e.g. of the conduction band (CB) onset, the bias-dependent STM appearance of the shamrock maxima and the work function of the surface, confirm our earlier assignment of the (√3×√3)R30° phase to the nano-pyramidal model. Moreover, we show that the charge redistribution induced by the screening at this Cu-deficient termination substantially differs from the one at stoichiometric and oxygen-deficient surfaces, with direct consequences on surface band bending and surface reactivity.

2. Experimental and computational methods

2.1 Experimental methods

The experiments have been carried out in an ultrahigh-vacuum chamber (UHV, p ~ $2*10^{-10}$ mbar) equipped with a liquid-nitrogen cooled STM and common surface-science tools for sample preparation and analysis. Electrochemically etched gold tips were used for STM imaging; the differential conductance (dI/dV) spectra were acquired with lock-in technique at 14 mV modulation bias and ~1.8 kHz. The Cu_2O films were prepared by depositing ~10 ML of high-purity copper onto an Au(111) single crystal, followed by an oxidation in 50 mbar O_2 at 450 K.[17] This high-pressure oxidation scheme turned out to be crucial to prepare Cu_2O films with bulk-like properties, while only monolayer oxides could be grown at UHV-compatible O_2 pressures below 10^{-5} mbar.[19] To promote film crystallization, the samples were post-annealed in front of an oxygen nozzle at p ~ 10^{-4} mbar and 650 K. The so prepared films displayed a sharp, hexagonal LEED pattern, comprising the fundamental (1×1) reflexes of bulk-type $Cu_2O(111)$ and a (√3×√3)R30° superstructure (Figure 1). The Au(111) spots could not be resolved anymore due to the high oxide thickness. The stoichiometry of the oxide layer was determined by X-ray photoelectron spectroscopy to be Cu_2O.[17,20] No difference could be detected in the diffraction, spectroscopy and microscopy response of the supported Cu_2O films used here and single-crystal data from the literature.[12,13]

2.2 Computational method

Calculations have been performed within the DFT framework implemented in VASP.[21,22] The hybrid HSE06 approximation to the exchange-correlation functional (¼ of the short-range Hartree–Fock exact exchange) has been used as to improve the description of the Cu_2O electronic structure.[23] Indeed, the calculated HSE band gap (1.96 eV) is significantly larger than the GGA gap of 0.4 eV and close to the experimental value (2.15 eV).[1] The interaction of valence electrons with ionic cores is described within the projector augmented wave method.[24] Standard copper and soft oxygen pseudopotentials provided by VASP are used, enabling a complete structural relaxation at the hybrid level for all considered systems. The use of the full (energy cut-off of 400 eV) rather than the soft (energy cutoff of 270 eV) oxygen pseudopotential yielded differences in the bulk Cu_2O lattice parameter and (1x1) surface energies smaller than 0.01 Å and 0.002 eV/Å, respectively.

The present computational settings closely resemble those in Ref. [18], but thicker slabs have been used to better account for the propagation of surface perturbations into the subsurface region. The employed $Cu_2O(111)$ slabs are composed of five O-4Cu-O trilayers at the calculated bulk in-plane lattice parameter (6.07 Å). To improve the convergence as a function of slab thickness, asymmetric slabs with one bare and one fully hydroxylated termination are used. The latter is the stoichiometric $Cu_2O(111)$ surface with three dissociated water molecules per $(\sqrt{3}\times\sqrt{3})R30°$ surface unit cell. In all calculations, the slabs are separated by at least 10 Å of vacuum and dipole correction is applied. The Brillouin zone of the $(\sqrt{3}\times\sqrt{3})R30°$ unit cell is sampled with a (2×2) Monkhorst-Pack k-point grid.[25] Atomic coordinates of all atoms are relaxed until residual forces drop below 0.02 eV/Å. Our simulations of the STM/STS images rely on the Tersoff-Haman formalism,[26] using $5\cdot10^{-5}$ e/Å^3 for the isodensity surface and 0.4 V for the width of the energy window around the bias tension. Atomic charges are estimated with the partition scheme proposed by Bader,[27,28] and atomic configurations are plotted with VESTA.[29]

3 Results

In this section, we report STM conductance measurements probing the electronic structure and work function of the (1×1) and $(\sqrt{3}\times\sqrt{3})R30°$ reconstructed $Cu_2O(111)$ surfaces and compare the results to the characteristics revealed from hybrid DFT calculations.

3.1 Surface terminations

The Cu_2O films on Au(111) are characterized by large flat terraces with (111) orientation, separated by 2.5 Å high step edges (Fig. 1a). At the atomic scale, the surface is homogenously covered with a hexagonal network of shamrock protrusions of 1.5 Å height and 10.5 Å periodicity. They are arranged in a $(\sqrt{3}\times\sqrt{3})R30°$ pattern as also detected in the LEED data (Fig. 1b). In open patches

between the shamrock regions, a network of honeycomb rings with (1×1) periodicity is observed on the surface (Fig. 1c).

Our previous study has demonstrated that this (1×1) ring pattern corresponds to the Cu-deficient surface (CuD in Fig. 2a), realized by removing all coordinatively unsaturated Cu_{CUS} ions from the stoichiometric (1×1) termination (ST).[18] The shamrock reconstruction, on the other hand, was unambiguously assigned to Cu_4O nano-pyramids bound to the center of every third Cu-O six-member ring. The nano-pyramids are composed of three Cu adatoms, which saturate the under-coordinated O_{CUS} ions of the stoichiometric surface. They are capped by an O atom and have an additional copper sitting below the nano-pyramid in the original Cu_{CUS} position (PY in Fig. 2a). The Cu_{CUS} ions in the neighboring rings are missing, which renders this configuration globally Cu-deficient (one missing Cu atom per (√3×√3)R30° unit cell). STM simulations based on this model revealed a very convincing match to the experimental data, both with respect to the shamrock location within the Cu-O rings and the orientation of its lobes towards the O_{CUS} species.[18]

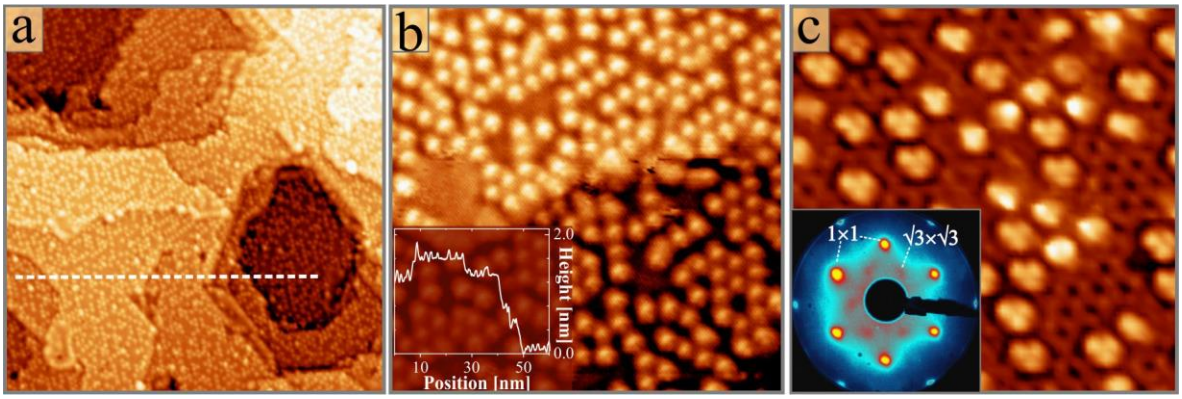

Fig. 1: (a) Overview STM image of the Cu_2O/Au(111) film covered with the (√3×√3)R30° reconstruction (75×75 nm^2, U_B = 2.1 V, I = 50 pA). **(b)** Higher resolved image showing the hexagonal shamrock pattern (20×20 nm^2). The inset depicts a height profile taken along the dashed line in panel (a). **(c)** Cu_2O region that is dominated by the (1×1) termination and shows a reduced shamrock density (11×11 nm^2). The trifold symmetry of the individual shamrocks is clearly resolved. The inset exhibits a LEED measurement acquired at 37.5 eV electron energy.

In addition, our hybrid DFT calculations revealed that the PY termination is thermodynamically favored in a wide range of accessible oxygen chemical potentials and more stable than the unreconstructed ST and the CuD surface, Fig. 2b. We note that a defective pyramidal configuration, with missing Cu_{CUS} atoms below the nano-pyramids (PY-Cu_{CUS}), is also relatively low in energy at O-rich conditions. Conversely, the formation of subsurface O vacancies located below the Cu_4O nano-pyramids (PY-O_{ss}) becomes accessible in an O-poor environment, while surface O defects remains thermodynamically unfavorable at all conditions.[18] This contradicts the widespread O-vacancy model that aims at explaining the (√3×√3)R30° reconstruction by a stoichiometric surface with 1/3 of the surface O_{CUS} being removed (ST-O_s). This surface structure is by far less stable than the preferred PY termination and out of scale in Fig. 2b.

In the following, we compare the dI/dV spectral signatures of (1×1) and (√3×√3)R30° surfaces with the calculated electronic properties of the two low-energy CuD and PY terminations.

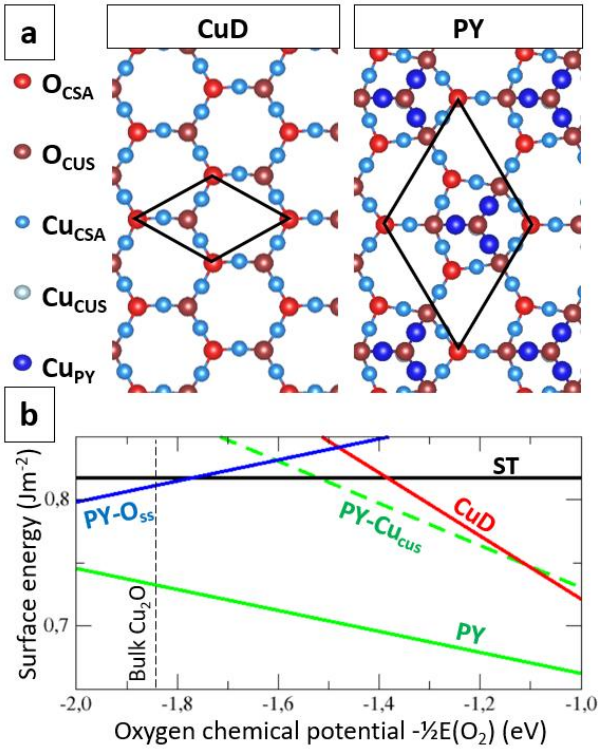

Fig. 2: **(a)** Atomistic representation of the (1×1) Cu-deficient (CuD) and the (√3×√3)R30° nano-pyramidal (PY) termination of the Cu_2O(111) surface. Different colors indicate coordinatively saturated (CSA) and unsaturated (CUS) surface ions, as well as the Cu cations in the nano-pyramids. The unit cells are indicated by black lines. **(b)** Calculated HSE energies of the energetically preferred Cu_2O(111) terminations plotted as a function of the oxygen chemical potential referred to an O_2 molecule. The vertical dashed line marks the stability limit of bulk Cu_2O.

3.2 STM Conductance spectroscopy and LDOS signature

Conductance spectra of the Cu_2O(111) surface are governed by a highly asymmetric band gap, extending from 0.0 to 2.0 V sample bias as expected for a p-type material.[17] The CB edge shows up by a sudden increase of the dI/dV signal that is more pronounced on the (√3×√3)R30° than the (1×1) reconstructed surface (Fig. 3a). A similar observation is made in dI/dV maps taken at the band onset (Fig. 3b). The shamrock maxima of the (√3×√3)R30° reconstruction develop measurable signals already at 2.1 V and are imaged with a unique sombrero shape, i.e. a bright center surrounded by a dark ring. At increasing bias, they show diminishing dI/dV intensity until the contrast inverts and the shamrocks appear darker than the environment at 3.0 V. Notably, a few individual maxima exhibit a deviating dI/dV response and show an inverted (dark) dI/dV signature at the CB onset (Fig. 3c). This difference suggests a deviating composition and/or charge state of those shamrock units. The small (1×1) patches, on the other hand, exhibit low dI/dV contrast directly at the CB onset and turn bright only above 4.0 V bias (Fig. 3b).

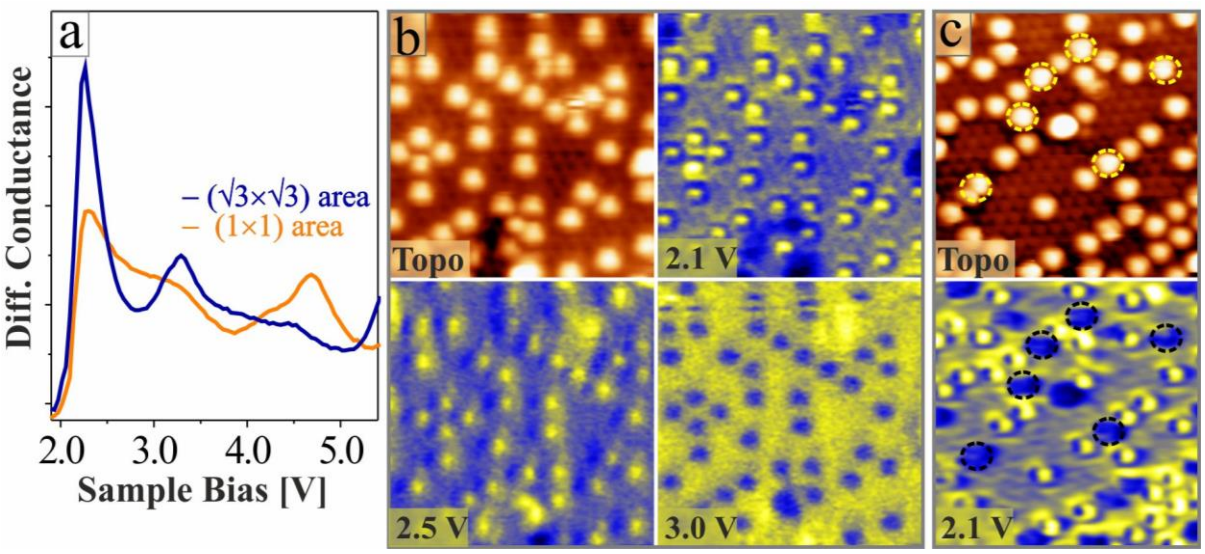

Fig. 3: **(a)** Differential conductance (dI/dV) spectra covering the conduction band in (√3×√3)R30° and (1×1) regions of the Cu_2O surface. **(b)** Topography and conductance maps of the Cu_2O(111) surface at the given bias values (I = 50 pA, 12×12 nm^2). The shamrocks appear with a unique sombrero shape at the band onset and flip to negative contrast at 3.0 V. **(c)** Topography and conductance map of a similar surface region, yet with unusual shamrock units that develop dark dI/dV contrast instead of the sombrero shape at 2.1 V (yellow circles, I = 50 pA, 12×12 nm).

The measured characteristics can be confronted with the Cu-projected local density of states (LDOS) at the CuD and PY terminations, Fig. 4a. In both cases, the Fermi level, $E_{F,}$ intersects the surface valence band (VB), as expected for these two Cu-deficient surfaces. At the onsets of the CB, on the other hand, the LDOS of the CuD and PY terminations significantly differ. A large LDOS peak at 2.5 eV is found at the PY surface, but not at the CuD termination. The existence of this LDOS peak is linked to the presence of surface Cu_{CUS} atoms below the nano-pyramids. Indeed, the same peak exists (at slightly lower energy) at the ST termination as well, where all surface Cu_{CUS} atoms are present. Conversely, it is absent at the reconstructed PY-Cu_{CUS} termination that lacks the Cu_{CUS} atoms below the nano-pyramids (Fig. 4a).

An interesting consequence of the LDOS structure at the PY termination is the pronounced sensitivity of dI/dV intensity maps to the bias voltage. Here, the dip in the Cu-projected LDOS at ~3.0 eV produces a sombrero shape of the shamrock maxima in the dI/dV simulations, Fig. 4b, in agreement with the experimental data shown in Fig. 3b. Indeed, while the copper atoms produce only weak contrast at 3.0 eV, the capping O atoms appear bright due to their elevation above the surface. This distinct contrast signature can be used to analyze the nature of the shamrock units. For example, the sombrero shape is not detected for a PY-Cu_{CUS} species that lacks the Cu_{CUS} ion below the nano-pyramid and appears with inverted contrast in the dI/dV simulations (Fig. 4c). A PY-Cu_{CUS} configuration thus offers a possible explanation for the unusual shamrock maxima detected in Fig. 3c.

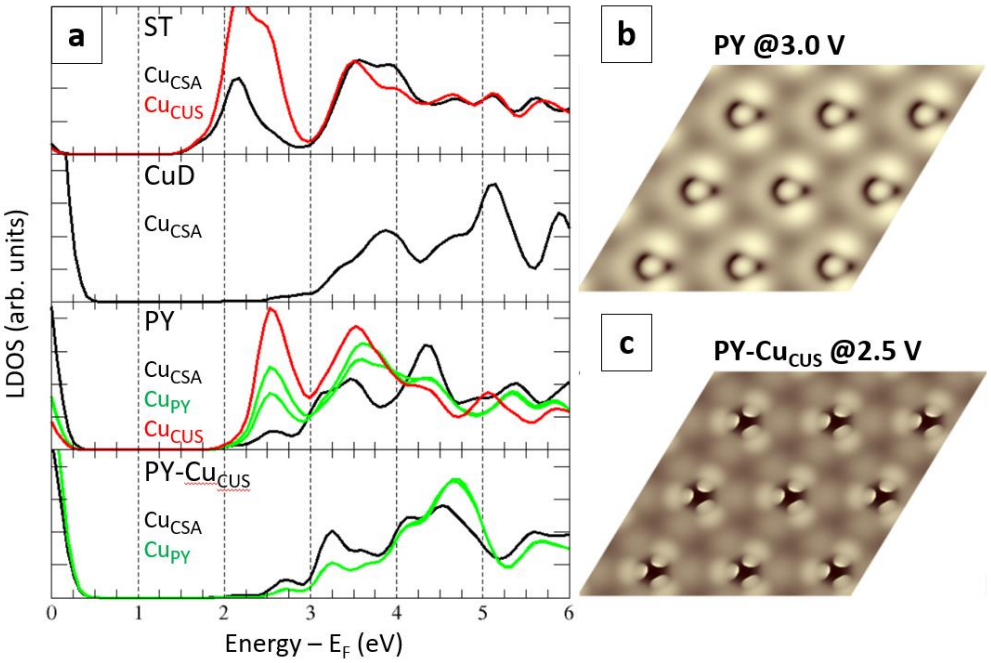

Fig. 4: **(a)**: LDOS of the conduction band region, projected on inequivalent surface Cu atoms at the ST, CuD, PY, and PY-Cu_{CUS} terminations. Simulated dI/dV images of **(b)** the PY and **(c)** the PY-Cu_{CUS} termination at 3.0 and 2.5 V sample bias, respectively.

3.3 Work function, electrostatic dipole and charge distribution

X-ray photoelectron spectroscopy could not be applied to determine the work function φ of the two terminations, as they always coexist on the Cu_2O surface. Moreover, the (√3×√3)R30° termination was found to be unstable upon X-ray exposure, as deduced from a vanishing LEED pattern.[14] Local information could still be acquired by evaluating the field emission resonances (FERs) in the STM junction.[30] FERs are bound electronic states in the potential well formed between vacuum barrier and sample surface. Their energy position E_n can be approximated with a triangular particle-in-a-box model (Eq.1): $E_n = \varphi + (\frac{3\pi\hbar eF}{2\sqrt{2m}})^{\frac{2}{3}} \cdot n^{\frac{2}{3}}$ with F the tip-sample electric field and m the free electron mass.[31] The first resonance is often neglected in the fitting procedure, as it undergoes a considerable downshift due to the image potential felt by the electrons in proximity to the sample surface. Two representative FER spectra for the (1×1) and (√3×√3)R30° terminations are depicted by orange and blue lines in Fig. 5a, respectively. The (1×1) spectrum starts with the 1st FER at 6.5 V, followed by three more states below 10 V. The 1st resonance in the (√3×√3)R30° spectrum, on the other hand, locates at 5.6 V, while higher states are strongly convoluted with the maxima of the (1×1) curve. The intermixing of the two curves results from the small size of (1×1) and (√3×√3)R30° domains combined with the low spatial resolution of STM at elevated bias. To extract a more realistic shape, we have subtracted the (1×1) from the (√3×√3)R30° data, which yields the broken line in Fig. 5a. So obtained resonance energies were then fitted to Eq. 1, yielding φ values of 5.85 and 5.4 eV for the (1×1) and (√3×√3)R30° surface, respectively. While the absolute values suffer from an error margin of ±0.5 V, given the low number of resonance states,[31] the work function difference is

reliably deduced for the two terminations. To substantiate our finding, dI/dV maps have been recorded at the bias positions of the FERs (Fig. 5b). Despite the poor spatial resolution of the high-bias maps, the enhanced dI/dV signal at 5.6 V in the shamrock regions and at 6.6 V in the encircled (1×1) patch is clearly discernable. Evidently, the (√3×√3)R30° surface exhibits lower FERs and has a lower work function than the (1×1) termination.

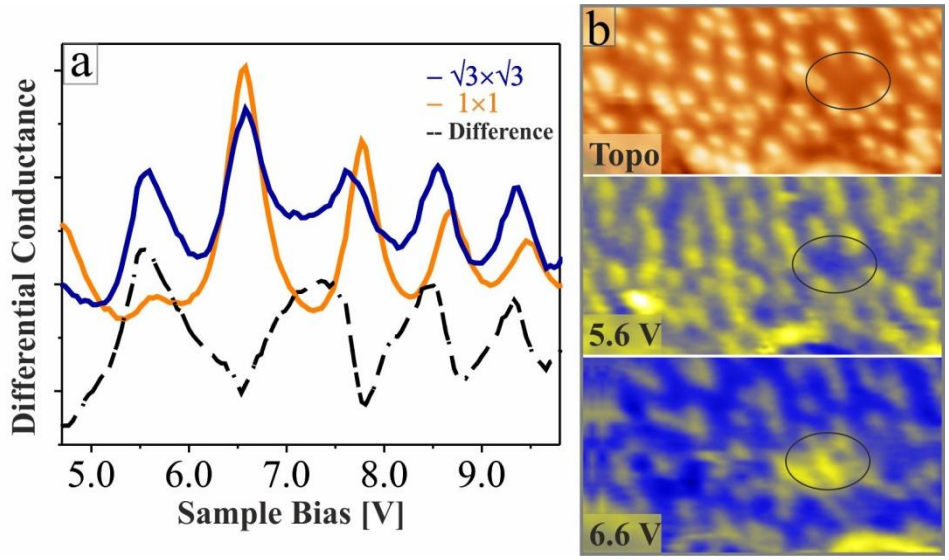

Fig. 5: **(a)** Series of FERs measured on (√3×√3) and (1×1) patches of $Cu_2O(111)$. The black curve shows the difference of the two spectra. By fitting the maxima to a triangular 'particle-in-the-box' potential, the work-function difference of the two phases is determined to be 0.45 V. **(b)** STM topographic and dI/dV images of a $Cu_2O(111)$ area taken in the bias window of the FERs (15×7 nm^2). The (√3×√3)R30° regions show up with high intensity at 5.6 V, while the (1×1) patch turns bright at 6.6 V due to the upshifted resonance position.

Calculated work functions are reported in Fig. 6a. As to broaden the perspective beyond the CuD and PY terminations, we have included the low-energy PY-Cu_{CUS} configuration without Cu_{CUS} below the nano-pyramids, the stoichiometric (ST) surface and the oxygen vacancy model that is often used to rationalize the (√3×√3)R30° reconstruction (ST-O_s). The obtained work functions span a large range from 5.1-5.4 eV for ST and ST-O_s up to 5.5-5.9 eV for the PY, PY-Cu_{CUS}, and CuD terminations. We note that the values calculated for CuD and PY (5.9 and 5.5 eV, respectively) are in good agreement with results of our FER measurements, which further validates our configuration assignment.

Interestingly, the calculated work function varies monotonically with the surface chemical composition (Fig. 6a). Compared to stoichiometric Cu_2O, three, two, and one Cu atoms are missing per surface unit cell in CuD, PY-Cu_{CUS}, and PY configurations, respectively, while the ST-O_s lacks one O atom, being equivalent to two excess copper. The work function follows this trend according to φ(CuD) > φ(PY-Cu_{CUS}) > φ(PY) > φ(ST) > φ(ST-O_s). Moreover, it scales linearly with the total surface dipoles, as evaluated via $\Sigma_i q_i z_i$ from the calculated atomic positions z_i and surface charges q_i. Thus, the surface electronic characteristic can be confidently analyzed with the help of calculated trilayer charges for the respective structures, as reported in Fig. 6b.[32]

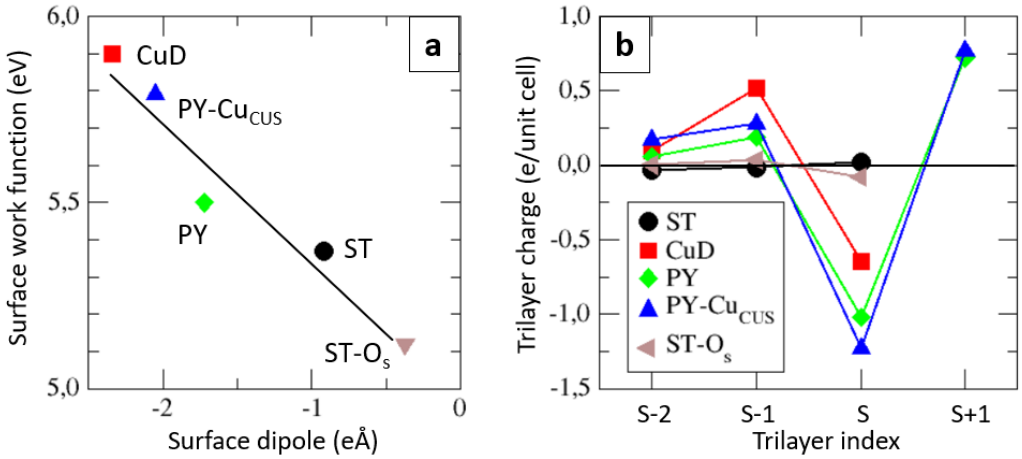

Fig. 6: **(a)** Work functions of the various $Cu_2O(111)$ terminations as a function of their total surface dipoles. **(b)** Calculated charge profiles of successive trilayers in slabs with the given surface terminations. Indices S, S-1, and S-2 refer to the surface, subsurface, and sub-subsurface trilayer, respectively. S+1 includes all atoms above the surface plane of the ST surface.

We find that the charge profile of the stoichiometric termination ST is essentially flat, as it can be expected from its charge neutrality and small surface dipole. A comparably flat profile is obtained for the ST-O_s termination as well, showing that surface oxygen vacancies do not produce any considerable electron redistribution within the subsurface trilayers. Conversely, significant modifications of the trilayer charges occur at the Cu-deficient terminations. The modifications consist of a positive charging of the subsurface layers, which is particularly strong at S-1 but propagates to S-2 and beyond. These positive charges are balanced by the negatively charged surface trilayers (S plus S+1). The resulting large negative dipole moment is responsible for the calculated work function increase of these terminations. Such qualitative difference in the charge profiles between Cu-deficient and Cu-rich terminations suggests a very different screening mechanism associated with missing copper and oxygen atoms.

4 Discussion

To get a deeper insight on how the surface stoichiometry governs surface dipole and work function, this section considers the electronic consequences of surface Cu- and O-deficiencies in more details. We show that the screening mechanism of the two defect types is qualitatively different, leads to contrasting band bending effects, and impacts differently the position of electronic states at the surface.

4.1 Screening effects

Considering the similarity of the charge profiles of all Cu-deficient terminations (CuD, PY-Cu_{CUS} and PY), Fig. 6b, we will restrict our analysis of Cu-deficiency to the CuD case and compare it to the O-deficiency at the ST-O_s termination. Surface neutrality of the CuD termination (negative formal charge) is achieved by the creation of holes in the VB, as evidenced in the LDOS plots

projected onto the Cu ions, Fig. 7a. The Fermi level intersects the VB not only at the surface but also in deeper trilayers, showing that the positive screening charges propagate subsurface. The calculated atomic charges confirm that mainly Cu ions participate to this hole propagation, whereas the oxygen charges remain essentially unaltered. While such a delocalized screening may indeed be expected in a strongly covalent oxide with small band gap, the propagation of holes towards subsurface cations is promoted here by the Mott-Hubbard nature of Cu_2O with its Cu-3d type VB top. In contrast to other oxides, like NiO,[33] ZnO,[34] and Cr_2O_3,[35] in which a cation vacancy shifts an empty state upward from the VB into the gap, the metallization of several trilayers at the Cu_2O surface, as seen by the Fermi level position inside the VB, reflects the specific screening behavior at Cu-deficient terminations.

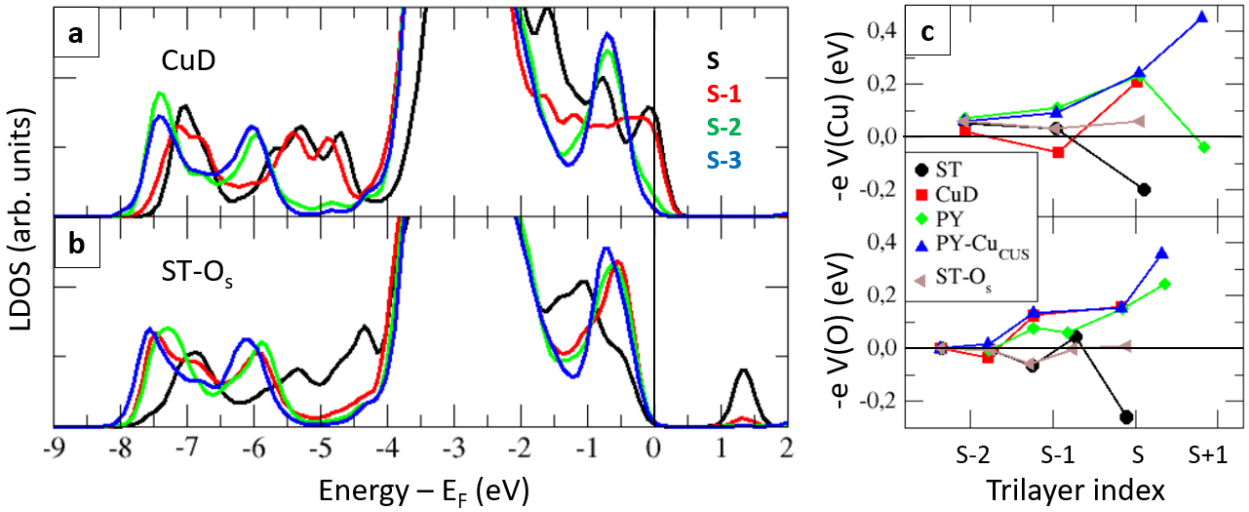

Fig. 7: LDOS of **(a)** the CuD and **(b)** the ST-O_s terminations projected on Cu atoms located in S, S-1, S-2, and S-3 trilayers. **(c)**: Relative positions of atomic levels at the saturated O (-eV(O)) and Cu ions (-eV(Cu)) in these trilayers at the indicated surface terminations.

In contrast, surface neutrality of the ST-O_s termination (positive formal charge) is achieved by the excess electrons left behind by the missing neutral oxygen atom. In the present case, they remain localized on the three Cu neighbors nearest to the vacancy and, to a smaller extent, on the three surface Cu_{CUS}, and no screening charges propagate towards deeper layers. Indeed, these six atoms experience an important charge reduction, which entirely screens the missing oxygen charge and leads to charge neutrality of the surface trilayer (Fig. 6b). Moreover, Fig. 7b evidences that the filled vacancy state does not lie in the gap, but is rather in resonance with the VB, in contrast to the response of many other oxides, such as MgO, ZnO, or TiO_2.[36,37,38] The strong downward shift of the filled CB state across the entire band gap into the VB is due to the comparatively large reduction of the Madelung potential in Cu_2O, where neighboring cations lose one of their two O partners upon vacancy formation. Similar results were reported for Cu_2O,[13,39] but also for the isostructural Ag_2O.[40]

4.2 Band bending

We have shown that the screening mechanism strongly affects the charge distribution at the surface and thus the magnitude of surface dipole and work function. It also drives the relative positions of electronic states and the resulting band bending effects in the surface vicinity. Considering that Cu_2O is a promising material for photoelectrochemical energy conversion, the position of the band onsets at the surface is of utmost importance since it governs the ability of the oxide to drive either hydrogen or oxygen evolution reactions.[41,42] To estimate the strength of surface electronic effects we have calculated the electron potential at oxygen and copper sites (-eV(O) and -eV(Cu), respectively) in successive trilayers, which is representative for the positions of both, the core levels and the center of gravity of the VB LDOS. Two different effects control these positions in coordinatively saturated and unsaturated ions.

Regarding coordinatively saturated ions, the -eV(O) and -eV(Cu) profiles in the copper-deficient CuD, PY-Cu_{CUS} and PY configurations, Fig. 7c, are characterized by a similar progressive upward shift when moving from the S-2 trilayer (serving as bulk reference) toward the surface. The largest cumulated upshift of +0.4 eV is found in the S trilayer of the PY-Cu_{CUS} termination. In contrast, the -eV(O) and -eV(Cu) profiles are essentially flat at the O-deficient ST-O_s configuration, and reveals even a downward shift in the surface trilayer (S) of the ST configuration. This qualitatively different behavior at Cu-poor and O-poor terminations can be directly linked to their peculiar charge distributions, Fig. 6b, driven by the delocalization of the screening charges into the subsurface trilayers.

An additional upward shift of atomic levels occurs at the coordinatively unsaturated ions (not shown in Fig. 7c) and arises from a reduced electrostatic potential due to missing neighbors. The shift is largest for the O_{CUS} atoms (1.15±0.1 eV compared to fully-coordinated O species), but hardly varies among the different terminations. Only exception is the capping O atom in the PY configuration (+0.7 eV), where the positively charged Cu_{CUS} atom below the nano-pyramids reduces the upward shift. The interplay of screening and under-coordination effects now produces a variety of energy positions for the surface O_{CUS} states. We find that the -eV(O_{CUS}) are shifted by about +1.0 eV at the PY and ST termination and by 1.2 eV at the CuD and ST-O_s ones. The largest upshift of +1.6 eV is however revealed for PY-Cu_{CUS}, where the strongest screening effect (+0.4 eV) coincides with a large contribution due to oxygen under-coordination (+1.2 eV).

Before concluding it is worth pointing out several important differences in the electronic signatures of the CuD and PY terminations of Cu_2O(111), as corroborated by the present experimental results, and those of the ST and ST-O_s configurations that are often used to rationalize the (1×1) and ($\sqrt{3}\times\sqrt{3}$)R30° surfaces in the literature. The first one is the presence of empty states in the oxide band gap at the ST-O_s termination, Fig. 7b. Our experiments do not evidence such states, which strongly supports an assignment to the Cu-deficient PY termination where unoccupied gap states are absent. Second, the Cu-deficient nature of CuD and PY terminations is also reflected in a larger calculated work function (5.9 and 5.4 eV, respectively) with respect to the ST and ST-O_s surfaces (5.3 and 5.1 eV). While the former two values are in good agreement with the experimental data, the latter are clearly too small. And third, we stress that the low formation energy of the CuD and

PY configurations is consistent with an oxide preparation in O excess and at high temperature ($p \sim 10^{-4}$ mbar, 650 K), which favors the development of Cu-deficient terminations close to thermodynamic equilibrium.

5 Conclusion

By combining high-resolution STM measurements and numerical simulations based on a hybrid DFT approach, we have investigated the electronic properties of the (1×1) and (√3×√3)R30° Cu_2O(111) surfaces. We have shown that the experimental signatures, such as the onset of the CB, the sombrero shape of surface protrusions and the work function, match very convincingly the calculated electronic characteristics of the (1×1) CuD and (√3×√3)R30° PY terminations. The present results thus substantially strengthen our previous assignment that was solely made on the basis of structural and energetic arguments.

On a more fundamental level, we show that the electronic characteristics of these two terminations are largely driven by their Cu-deficient nature. Indeed, we find that the screening charges (holes) at these surfaces delocalize toward subsurface regions, resulting in a large negative surface dipole, a work function increase and a positive band bending. This is in stark contrast to O-deficient surfaces, at which the screening charges (electrons) remain localized in vicinity of the O defects, generate a smaller surface dipole and work function and largely suppress band-bending effects. Finally, we show that the nature of screening combined with atom under-coordination also impacts the relative positions of electronic states at the very surface. In this perspective, the proposed Cu-deficient Cu_2O(111) surface models, in which low-coordinated Cu_{CUS} ions are absent, will drastically change common perceptions of the surface reactivity of cuprous oxide.

Acknowledgments: NN acknowledges financial support from the DFG grant Ni 650-5 ‘Towards an atomic-scale understanding of ideal, defective and doped cuprous oxide surfaces and interfaces.

6 References

[1] Meyer B K et al. 2012 *Phys. Status Solidi* **249** 1487–1509

[2] Ito T and Masumi T 1997 *Journal of the Physical Society of Japan* **66** 2185–2193

[3] Zheng Z, Huang B, Wang Z, Guo M, Qin X, Zhang X, Wang P and Dai Y 2009 *J. Phys. Chem. C* **113** 14448–14453

[4] Kakuta S and Abe T 2009 *Solid State Sci.* **11** 1465–1469

[5] Chatterjee S, Saha S K and Pal A J 2016 *Sol. Energy Mater. Sol. Cells* **147** 17–26

[6] Besharat Z, Halldin Stenlid J, Soldemo M, Marks K, Önsten A, Johnson M, Öström H, Weissenrieder J, Brinck T and Göthelid M 2017 *J. Chem. Phys.* **146** 244702

[7] Karagoz B, Blum M A and Head A R 2021 *J. Phys. D: Appl. Phys.* **54** 194002

[8] Zhang R, Liu H, Zheng H, Ling L, Li Z and Wang B 2011 *Appl. Surf. Sci.* **257** 4787–4794

[9] Riplinger C and Carter E A 2015 *J. Phys. Chem. C* **119** 9311–9323

[10] Bendavid L I and Carter E A 2013 *J. Phys. Chem. B* **117** 15750–15760

[11] Schulz K H and Cox D F 1991 *Phys. Rev. B* **43** 1610–1621

[12] Önsten A, Göthelid M and Karlsson U O 2009 *Surf. Sci.* **603** 257–264

[13] Zhang R, Li L, Frazer L, Chang K B, Poeppelmeier K R, Chan M K Y and Guest J R 2018 *Phys. Chem. Chem. Phys.* **20** 27456–27463

[14] Leuenberger D, Zabka W D, Shah O F R, Schnidrig S, Probst B, Alberto R and Osterwalder J 2017 *Nano Lett.* **17** 6620–6625

[15] Nilius N, Fedderwitz H, Groß B, Noguera C and Goniakowski J 2016 *Phys. Chem. Chem. Phys.* **18** 6729–6733

[16] Soon A, Todorova M, Delley B and Stampfl C 2007 *Phys. Rev. B* **75** 125420

[17] Gloystein A and Nilius N 2020 *J. Phys. Chem. C* **124** 28605-28613

[18] Gloystein A, Nilius N, Goniakowski J and Noguera C 2020 *J. Phys. Chem. C* **124** 26937−26943

[19] Gloystein A and Nilius N 2019 *J. Phys. Chem. C* **123** 26939-26946

[20] Poulston S, Parlett P M, Stone P and Bowker M 1996 *Surf. Inter. Anal.* **24** 811–820

[21] Kresse G and Hafner J 1993 *Phys. Rev. B* **47** 558−561

[22] Kresse G and Furthmüller J 1996 *Phys. Rev. B* **54** 11169−11186

[23] Heyd J, Scuseria G E and Ernzerhof M 2003 *J. Chem. Phys.* **118** 8207−8215

[24] Kresse G and Joubert D 1999 *Phys. Rev. B* **59** 1758−1775

[25] Monkhorst H J and Pack J D 1976 *Phys. Rev. B* **13** 5188−5192

[26] Tersoff J and Hamann D R 1985 *Phys. Rev. B* **31** 805-813

[27] Bader R F W 1991 *Chem. Rev.* **91** 893-928

[28] Henkelman G, Arnaldsson A and Jónsson H 2006 *Computational Mat. Sci.* **36** 354-360

[29] Momma K and Izumi F 2011 *J. Appl. Cryst.* **44** 1272-1276

[30] Rienks E D L, Nilius N, Rust H P and Freund H-J 2005 *Phys. Rev. B* **71** 241404

[31] Kolesnychenko O Y, Kolesnichenko Y A, Shklyarevskii O I and van Kempen H 2000 *Phys. B: Condens. Matter* **291** 246−255

[32] Goniakowski J and Noguera C 2004 *Inter. Sci.* **12** 93–103

[33] Ferraria A M and Pisani C 2007 *J. Chem. Phys.* **127** 174711

[34] Janotti A and van de Walle C G 2007 *Phys. Rev. B* **76** 165202

[35] Carey J J, Legesse M and Nolan M 2016 *J. Phys. Chem. C* **120** 19160-19174

[36] Sterrer M, Heyde M, Nowicki M, Nilius N, Risse T, Rust H P, Pacchioni G and Freund H J 2006 *J. Phys. Chem.* **110** 46-49

[37] Kohan A F, Ceder G, Morgan D and Van de Walle C G 2000 *Phys. Rev. B* **61** 15019-15027

[38] Janotti A, Varley J B, Rinke P, Umezawa N, Kresse G and Van De Walle C G 2010 *Phys. Rev. B* **81** 085212

[39] Scanlon D O and Watson G W 2010 *J. Phys. Chem. Lett.* **1** 2582–2585

[40] Yin Y, Chen G, Duan X, Ye H, Jin W, Zhu Y and Wu Y 2016 *J. Appl. Phys.* **120** 215707

[41] Kudo A and Miseki Y 2009 *Chem. Soc. Rev* **38** 253–278

[42] Fernando C A N, Bandara T M W J and Wethasingha S K 2001 *Sol. Energy Mater. Sol. Cells* **70** 121–129